ASME Journal of Thermal Science and Engineering Applications
Online journal at:
https://asmedigitalcollection.asme.org/thermalscienceapplication

Mahadevan Ravichandran[1]
Laboratory for Product Development and Lightweight Design,
School of Engineering and Design,
Technical University of Munich,
Munich 85748, Germany
e-mail: mahadevan.ravichandran@tum.de

Johanna Winter
School of Medicine and Health,
Klinikum rechts der Isar,
Technical University of Munich,
Munich 81675, Germany
e-mail: johanna.winter@tum.de

Anton Dimroth
Forschungszentrum Jülich,
Jülich 52428, Germany
e-mail: a.dimroth@fz-juelich.de

Stefan Bartzsch
Institute of Radiation Medicine,
Helmholtz Zentrum Munich,
Munich 85764, Germany
e-mail: stefan.bartzsch@tum.de

Kim Melanie Kraus
School of Medicine and Health,
Klinikum rechts der Isar,
Technical University of Munich,
Munich 81675, Germany
e-mail: kimmelanie.kraus@mri.tum.de

Markus Zimmermann
Laboratory for Product Development and Lightweight Design,
School of Engineering and Design,
Technical University of Munich,
Munich 85748, Germany
e-mail: zimmermann@tum.de

Design and Validation Strategy for an X-Ray Target Subject to Ultra High Heat Flux Loading

Microbeam X-ray therapy is a promising cancer therapy that uses a high-power electron beam hitting a metallic target. For a clinical microbeam therapy X-ray source, an electron beam of a power of 1 MW onto a focal spot of 0.05 mm × 20 mm size is needed, with a penetration depth of 0.1 mm. This means a heat flux input of 1 TW/m^2, an order of magnitude higher than nuclear and medical applications. Numerical simulations based on surface and volumetric heat loading for such an electron beam are presented in this work. The local temperature around the focal spot is modeled in a lower-scale model with an element size of 10 μm and volumetric heat loading. This differs from the state-of-the-art simulations, in which electron beam loading is modeled as surface heat flux loads. The simulated temperature agrees with the mathematical estimates within an error of 10% while proving feasibility. A novel validation strategy is proposed to address the lack of available test facilities to replicate this extreme heat flux. The critical parameters describing the high-heat-flux-loading are identified as temperature, thermal strain, thermal stress, and strain rate. Scaled-down test specifications are determined to use a test facility of power less than 100 kW. With the verified simulation using the scaled-down test, it is proposed to establish the material's capability to withstand the concentrated 1 MW heat load without a 1 MW test facility. [DOI: 10.1115/1.4067589]

Keywords: biotechnology, heat and mass transfer, micro/nanoscale heat transfer, radiative heat transfer, very high-temperature heat transfer

1 Introduction

Radiation therapy has been a very important treatment method for cancer patients, with half the affected patients receiving this treatment. However, achieving a higher radiation dose for better treatment of cancer cells has been limited by the damage to normal tissues.[2] Microbeam radiation therapy (MRT) has shown superior normal tissue sparing at similar tumor control rates with the characteristic X-rays consisting of micrometer-sized beamlets separated by a few 100-μm-wide low dose regions [2]. The only X-ray sources that could deliver microbeam radiation therapy for patients currently are large third-generation synchrotrons owing to their high dose rate, and small beam divergence which enable spatial dose modulation on the micrometer scale. Hence, current research on MRT is primarily performed using synchrotron-generated X-rays at particle accelerator facilities of enormous scale. To make this concept of cancer therapy accessible to clinical treatment centers, new compact X-ray sources suitable to deliver MRT must be developed. These sources feature X-rays of a few hundred kiloelectron volts at dose rates of more than 100 Gy s^{-1} from a focal spot that does not exceed a few 10-mm widths. Conventional X-ray tubes make an electron beam impinge at the focal spot of a rotating anode, called the target, to generate X-rays. Targets are generally a metal disc with a layer of a tungsten alloy

[1]Corresponding author.
[2]Summer Heat Transfer Conference (SHTC2024), Hilton Anaheim, July 15–17, 2024 [1].

Manuscript received September 23, 2024; final manuscript received December 16, 2024; published online January 29, 2025. Assoc. Editor: Aaron P. Wemhoff.

close to its outer radius to absorb the electron beam. A representative arrangement is illustrated in Fig. 1. State-of-the-art X-ray sources used for X-ray imaging have a maximum power of the electron beam in the order of 120 kW and a focal spot size of 0.5–1 mm [3]. However, to enable clinical microbeam X-rays by preserving the unique spatial beam fractionation, line-focus X-ray tubes (LFXTs) could be a technical solution. The LFXT is characterized by a strongly eccentric focal spot and high tangential speeds (above 150 ms^{-1}) of the target, which enables the operation in the heat capacity limit [4]. Additionally, the electron beam power must be 1.5 MW, with a penetration depth above 100 μm to meet the dose rate requirement. The beam should be focused onto a focal spot of an area of 0.05 mm × 20 mm on the metallic target, where the shorter dimension is in the direction of the target tangential velocity [5]. It would be similar in architecture to the scaled-down prototypes for MRT X-ray sources under development but with higher power and tangential speed requirements [6]. This paper focuses on the development of the rotating metallic target for LFXT. Almost all of the power of the electron beam is absorbed by the metallic target and transformed into heat, and less than 2% of the electron energy is translated into X-rays [7]. One of the critical challenges in developing the target for this application is ensuring that the tungsten alloy layer and the carrier metal body, called the target body, can withstand the power of the impinging electron beam. In this work, we lay out the engineering requirements for such a target for MRT and identify the challenges involved in modeling and validation. Several numerical modeling methods are presented and compared, and a validation strategy is proposed.

2 Requirements

The operation of the line-focus X-ray tube in the heat capacity limit results in a volumetric heat transfer load of the absorbed electron beam on the rotating metallic target [4]. Using Monte-Carlo simulations, the absorption of electron beams over the depth of the material is calculated. This energy absorption distribution acts as the volumetric heat input for the metallic target. The Monte-Carlo simulations were done in the GEANT4 program with the absorption and scattering cross sections from the G4EmPenelope physics list. The material used was pure tungsten. Tungsten is used since it is the most commonly used material for electron absorption in X-ray tubes owing to its high melting point and high electron-to-photon conversion efficiency. The source power of electron beams is 1.5 MW [5]. Figure 2 shows the power absorbed along the depth of the material. The total power to be absorbed by the target is 1 MW over a depth of 100 μm. The remaining 0.5 MW of power is reflected back and not absorbed by the tungsten. Translated to a surface heat load, the absorbed power of 1 MW on an area of 0.05 mm × 20 mm leads to a flux of 1 TW m^{-2}.

To verify if tungsten alloy can withstand such a high-heat-flux-loading, the overall requirement of heat flux can be broken down

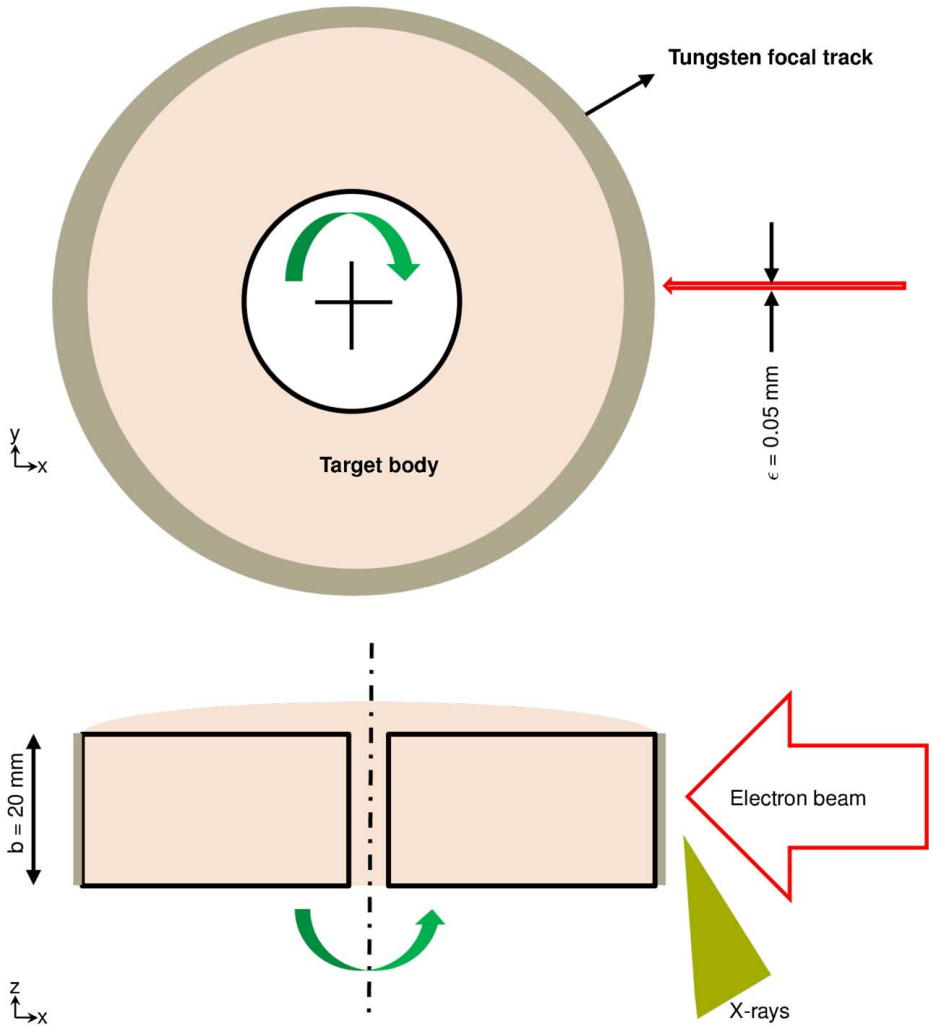

Fig. 1 Basic principle of X-ray generation with target front view and cross-sectional views and the electron beam length *b* and width ε needed for microbeam radiation therapy

into engineering requirements [8]. These three requirements ensure that the tungsten alloy and the target body do not melt due to heating and that the tungsten alloy can withstand the mechanical stresses due to thermal expansion. Accordingly, Eqs. (1) and (2) are the ratio of the melting point of the materials to their respective maximum temperatures. If the ratio is greater than 1, the maximum temperature is less than the melting point, and the requirement is considered met. For the mechanical failure requirement, the ratio of the material's ultimate strength to the maximum von Mises stress is used. If the ratio exceeds 1, the maximum stress is less than the ultimate strength, and the material will not break or crack. However, a reserve factor of 1.25 has been used as the requirement to prevent the materials from being right at the limit of failure. In this study, the focal track is assumed to fail only when a crack occurs on one cycle of operation. The number of cycles required and fatigue failure requirement for such a new application has not been established to be considered in this study.

$$r_{\text{meltft}} = \frac{\text{Melting point of focal track}}{\text{Maximum temperature of focal track}} > 1.25 \quad (1)$$

$$r_{\text{meltft}} = \frac{\text{Melting point of focal track}}{\text{Maximum temperature of target body}} > 1.25 \quad (2)$$

$$r_{ts} = \frac{\text{Ultimate strength of focal track}}{\text{Maximum von Mises stress of focal track}} > 1.25 \quad (3)$$

3 State-of-the-Art and Challenges

3.1 Modeling. Simulations of high-heat-flux-loading on metals have been performed for multiple applications like plasma-facing walls of nuclear fusion reactors, rocket and automotive engine walls, and electron beam loading [9,10]. Most of these applications consider the heat transfer to the metals as surface heat flux and evaluate thermal stress from the resulting thermal penetration and thermal gradients [11]. Among those, plasma-facing components (PFCs) of nuclear fusion reactors, often made of tungsten alloys, are known to have some of the highest heat flux loadings of the order of several MW m^{-2}. Research on PFCs has been primarily performed assuming that the thermal load acts as surface heat flux [12]. For rotating X-ray targets, the heat load at the small focal spot is distributed over the focal track within a short time because of the high rotation frequency [6]. Also, target structure simulations for X-ray tubes under electron beam loading have also been primarily done assuming that the thermal load is a surface heat flux or low-penetration heat load [13,14]. This assumption can also be attributed to the fact that the electron penetration depth is generally of the order of 5–10 μm [15]. Penetration depth is directly influenced by the electron beam energy [4]. For the line-focus X-ray tube, the penetration depth of electrons with an energy of up to 600 keV is an order of magnitude higher at around 100 μm, as shown in Fig. 2. Additionally, the surface heat flux, at 1 TW m^{-2}, is orders of magnitude higher than that of nuclear fusion reactors or conventional X-ray target applications [3,16]. Therefore, the method of thermal load application in numerical modeling is being reconsidered here. Three different numerical models using finite element methods (FEMs) are explained and applied in this work. Additionally, the numerical model results are compared with the results from the analytical model of temperatures, computed using heat transfer equations.

The heat deposited by the moving focal spot on the target will create thermal stresses in the focal track material due to thermal expansion around the focal spot. Closed-form solutions to such problems have been derived, solving for temperature and stress fields due to a moving heat source in a material. However, such models have been experimentally verified and used for heat source velocity ranges of only up to a few mm/s [17,18]. Some solutions suffer from the problem of singularity in the solution at the

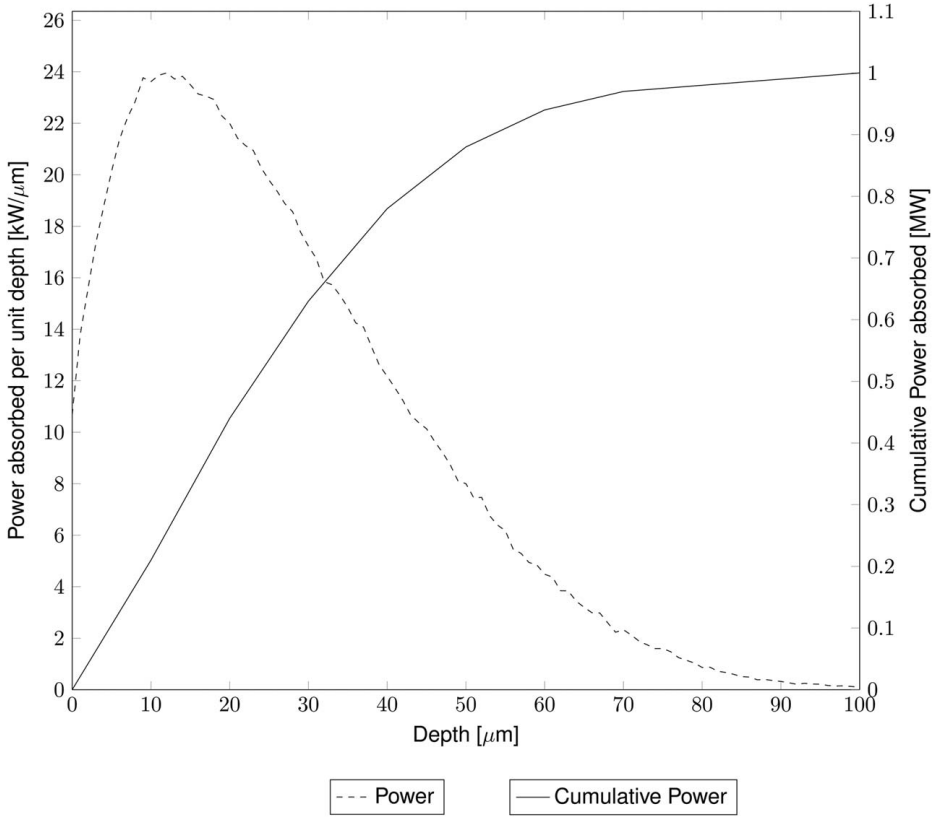

Fig. 2 Absorbed power over depth in the tungsten focal track

center of the heat source [19]. For microbeam radiation therapy, the tangential speed of the target of the line-focus X-ray tube is required to be above 150 ms^{-1}. Hence, the previously mentioned models are not suitable for the computation of local temperature distribution and stress fields. These quantities will be computed purely based on numerical models in Secs. 7.2 and 7.3 and validated with experimental methods as proposed in Sec. 7.1.

3.2 Validation. High-heat-flux-loaded components are generally tested with electron beams, other sub-atomic particle sources, or lasers. High-temperature, high-stress loaded components have been tested in equivalent testing conditions in special test facilities where the load applied is chosen to be comparable to the real loading scenario to replicate key parameters like thermal gradients [20]. Some of the highest heat flux-loaded applications, like the PFCs of nuclear fusion reactors, are tested in electron beam test facilities with a flux of up to a few tens of MW m^{-2} [12,16]. However, the flux range available in particle beam loading facilities is orders of magnitude lower than the flux requirement of 1 TW m^{-2} for the LFXT target [21]. Apart from the low heat flux in test facilities, a fundamental difference in the electron penetration depth between the test facilities and the line-focus X-ray tube needs to be considered. Today's high-heat-flux test facilities operate at a much lower penetration depth of less than 20 μm [22]. Thus, the existing high-heat-flux test facilities are unsuitable for testing the heat load with the heat flux in the order of TW m^{-2} and the penetration depth in the order of 100 μm for the target of the line-focus X-ray tube. Hence, to proceed with the validation of the target without the time delay for setting up a new electron beam test facility matching the specifications needed, a new validation strategy is needed, which will be explained in Sec. 7.

4 Basic Concept

The LFXT is based on the working principle of state-of-the-art X-ray tubes. The minimum requirements on geometric size, operational, and material parameters for an LFXT target have been derived in previous works [8]. From the feasible design domain, geometrical size, rotational frequency, and materials were chosen, considering manufacturing ease. The dimensions and the material details chosen are depicted in Fig. 3. The metallic target body is assumed to be made of titanium–zirconium–molybdenum (TZM) alloy, which is a commonly used high-temperature environment material made of titanium, zirconium, and molybdenum. The focal track is assumed to be made of tungsten. The radial thickness (X-direction) of the tungsten focal track is taken as 2 mm for the concept. Considering that only 0.1 mm of tungsten is needed for electron penetration, the added thickness is to ensure a uniform heat transfer to TZM. The tungsten focal track width (Z-direction) of 30 mm is also wider than the electron beam width of 20 mm, ensuring that the electron beam will stay within the tungsten surface even with minor variations in size and position. The focal track is enclosed by TZM for better heat transfer with contact in three surfaces with TZM instead of only radiation to the ambient environment. The outer radius of the target and rotational frequency are 0.4 m and 175 Hz, respectively, a combination that gives sufficiently high tangential speeds above 150 ms^{-1} for the LFXT to be operated in the heat capacity limit. The key thermal and mechanical properties of the materials used in this work are listed in Tables 1 and 2, respectively. The densities are taken as 19,500 kg m^{-3} and 10,220 kg m^{-3} for tungsten and TZM, respectively, and are assumed to be isotropic [23]. The target will receive an electron beam of a power of 1 MW for an operation time t_{op} of 1 s, sufficient to give a single radiation dose of about 100 Gy [5].

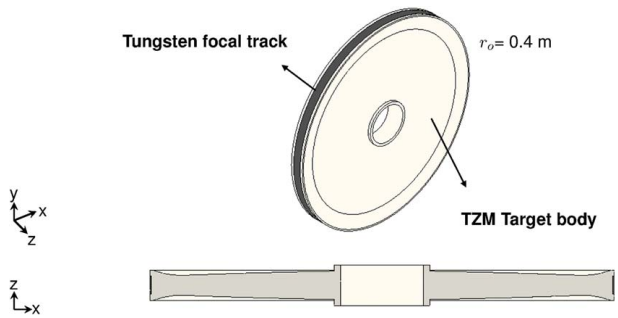

Fig. 3 Preliminary design of the target with isometric and cross-sectional views

5 Mathematical Modeling

5.1 Global Temperature. The target is assumed to be of the same uniform width b as the electron beam in the Z-direction, i.e., 20 mm. The target body made of TZM alloy, and the same width b, is assumed to get the entire electron beam power from the tungsten focal track as a uniform surface heat flux input on the surface in contact with the tungsten focal track. These simplifications help us to estimate the resulting maximum temperature using analytical solutions to Fourier's equation [26]. The maximum temperature of the TZM alloy, T_{TZM}, is calculated using Eqs. (4)–(7) [26]. This will be the maximum temperature the target body material TZM can reach, and the melting point of the TZM alloy should be sufficiently higher than this temperature as specified in Eq. (2). The term q' computed in Eq. (5) refers to the dimensionless intermediate heat flux term in the solution of Fourier's equation. A correction factor $\Delta T_{correction}$, calculated in Eq. (7), is added to account for the thickness of the tungsten focal track, in the radial or X-direction. The joint between the target body and the focal track is assumed to have zero thermal resistance. The maximum global temperature of the focal track, T_{surf}, is calculated in Eq. (8) by adding the correction factor to T_{TZM}. This will be the maximum homogeneous temperature the focal track material, tungsten alloy, can reach. The analytical solution for Fourier's equation assumes no radiation or convection and constant, isotropic material properties.

$$Fo = \frac{\alpha t_{op}}{(r_o)^2} \tag{4}$$

$$q' = 0.5\sqrt{\frac{\pi}{Fo}} - \pi\frac{1}{8.0} \tag{5}$$

Table 1 Material thermal properties at selected temperatures [23]

	Specific heat capacity, c_P (J kg^{-1} K^{-1})		Thermal conductivity, k (W m^{-1} K^{-1})	
Temperature (°C)	TZM	Tungsten	TZM	Tungsten
22	250	131	122	174
1000	300	157	109	119
2500	350	175	95	115

Table 2 Mechanical properties of tungsten at selected temperatures [24,25]

Temperature (°C)	Young's modulus, E (GPa)
22	420
1000	360
2500	160

$$T_{\text{TZM}} = \frac{Qr_o}{q' k_{\text{TZM}}} + T_o \tag{6}$$

$$\Delta T_{\text{correction}} = \frac{Qt_w}{k_w} \tag{7}$$

$$T_{\text{surf}} = T_{\text{TZM}} + \Delta T_{\text{correction}} \tag{8}$$

5.2 Local Temperature. The maximum temperature of the focal track T_{peak} is the temperature at the focal spot, acting as a local temperature peak in the focal track [6]. It is computed as the sum of the local temperature rise at the focal spot ΔT and the global maximum surface temperature of the focal track T_{surf} as in Eq. (9). This will be the maximum temperature of the focal track material tungsten and should satisfy Eq. (1). The local temperature rise ΔT is computed in Eq. (10) using the idea of the electron beams acting as volumetric heat input with the line-focus X-ray tube operating in the heat capacity limit [4].

$$T_{\text{peak}} = T_{\text{surf}} + \Delta T \tag{9}$$

$$\Delta T = \frac{P}{\upsilon \rho c_{Pw} db} \tag{10}$$

6 Numerical Modeling

Three different numerical models for FEM simulations will be presented in this section. The first two models are used to compute the global temperature distribution. One of the models will apply heat load on the surface as pure surface heat flux, while the other applies heat load as volumetric heat load. These models will both compute T_{TZM} and T_{surf}. These are two-dimensional axisymmetric models of the target in the Z–X plane. Since these global temperature models assume that the heat enters the target homogenously in the focal track, they cannot compute the local temperature rise at the focal spot and the peak local temperature at the focal spot. The model for local temperature modeling applies a moving volumetric heat load and will compute ΔT and T_{peak}. This is a two-dimensional model of the target in the X–Y plane. Since X-ray sources operate in ultra-high vacuum, heat transfer is simulated only through conduction in materials and radiation. To simplify the computation and not underestimate the maximum temperatures, constant room temperature emissivity values are used for all materials. The joint between the target body and the focal track is assumed to have zero thermal resistance as in the state-of-the-art simulations of X-ray targets [6,13].

6.1 Global Temperature Modeling: Surface Heat Input. This model is similar to the state-of-the-art high-heat-flux simulations and is being done for comparison. Hence, the heat is assumed to enter the target on the outer surface. A power of 1 MW is homogeneously applied on the outer surface area of the tungsten focal track for a duration of 1 s. The radiation boundary condition is applied on the outer surface, and an initial temperature of 22 °C is applied everywhere, corresponding to typical ambient conditions. The model is illustrated in Fig. 4.

6.2 Global Temperature Modeling: Volumetric Heat Input. This model applies the heat load as a volumetric heat load. The power of 1 MW is homogeneously applied to a circumferential ring with a thickness of 100 μm in tungsten, corresponding to the penetration depth of electrons for a duration of 1 s. Adding the load as homogenous heat input reduces the computation load drastically in the FEM model of a scale of 0.8 m. This has been done since the load is effectively the time-averaged heat input at the focal spot on a spinning target, and the significance of the non-homogeneity of electron penetration shown in Fig. 2 is lesser due to diffusion of heat over the load application time of 1 s. The radiation boundary condition is applied on the outer surface, and an initial temperature of 22 °C is applied everywhere, corresponding to typical ambient conditions. The model is illustrated in Fig. 5.

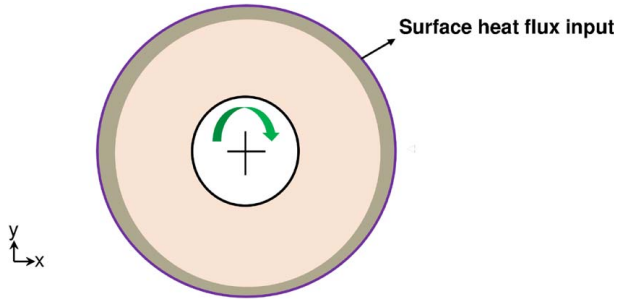

Fig. 4 Surface heat flux loading for global temperature modeling with heat loaded surface highlighted in the outer edge

6.3 Local Temperature Modeling: Moving Volumetric Heat Input. This model is used for the computation of local temperature rise ΔT and maximum temperature at the focal spot T_{peak}, and thermal expansion effects. This model is illustrated in Fig. 6. A small segment of the focal track is taken as the modeling domain, approximated as a rectangular block, with dimensions as shown in Fig. 6. A moving volumetric heat source is moved linearly across the domain in the positive X-direction at the speed of 440 m/s, corresponding to the tangential velocity of the metal

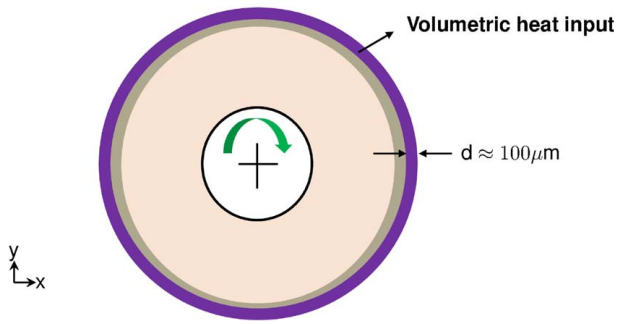

Fig. 5 Volumetric heat loading for global temperature modeling with the heat loaded volume highlighted near the outer edge

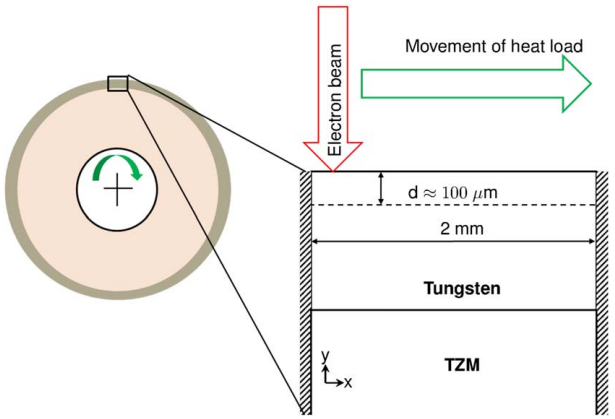

Fig. 6 Moving volumetric heat loading for local temperature modeling

target with an outer radius of 0.4 m, spinning at 175 Hz of rotational frequency. The volumetric heat source has a varying intensity in the depth of the material, in the radial direction, as observed in Fig. 2, and is moved along the domain, in the positive X-direction, 175 times for 1 s, corresponding to the rotational frequency. The heat source has a width of 50 μm with a homogeneous intensity in the direction of the movement, i.e., in X-direction. To replicate the target rotation, a time gap corresponding to the time of each rotation without an electron beam is replicated in the moving heat input. The domain is made to be such a small segment of the target to make the computation in a reasonable time since the model needs to be discretized to the order of micrometers to match the scale of the focal spot width of 50 μm, with a minimum mesh element size being 5 μm. This is based on the assumption of axisymmetry of temperature distribution so that the modeled temperature will represent the maximum temperature that lies at the center of the focal spot. Hence, the boundary conditions of the simulation are set to periodically repeat over the entire circumference of the target. The radiation boundary condition is applied on the outer surface, and an initial temperature of 22 °C is applied everywhere, corresponding to typical ambient conditions.

6.4 Results and Inferences. This section discusses the mesh independence of the numerical models and the requirements laid down by Eqs. (1) and (2) corresponding to the temperature requirements. The thermal stress-based requirement laid down by Eq. (3) needs modeling of thermal stress, which will be explained in Secs. 7.2 and 7.3, along with the experimental method to validate the same in Sec. 7.1.

6.4.1 Mesh Independency. To verify if the results from the numerical model are independent of the discretization used, the simulations were done for varying levels of discretization, and the results are summarized in Fig. 7 for global and local temperature models. The minimum grid size varies from 0.1 mm to 1 mm for the global temperature model and from 5 μm to 20 μm for the local temperature model. As the maximum temperature comparison between different discretization levels suggests, the variation due to discretization is smaller than 1% and convergence is of the order of 1×10^{-3} or less.

6.4.2 Global Temperature Modeling. The results of global temperature computation, explained in Secs. 6.1 and 6.2, are summarized in Table 3, by comparing the maximum global surface temperatures of tungsten, T_{surf}, and the maximum temperatures of the TZM alloy, T_{TZM}, at the end of the electron beam loading time of 1 s. As seen from the results, T_{TZM} at 1110 °C is far lower than the melting temperature of TZM alloy, which is over 2400 °C [23]. Thus, the requirement mentioned in Eq. (2) is satisfied. The values of T_{surf}

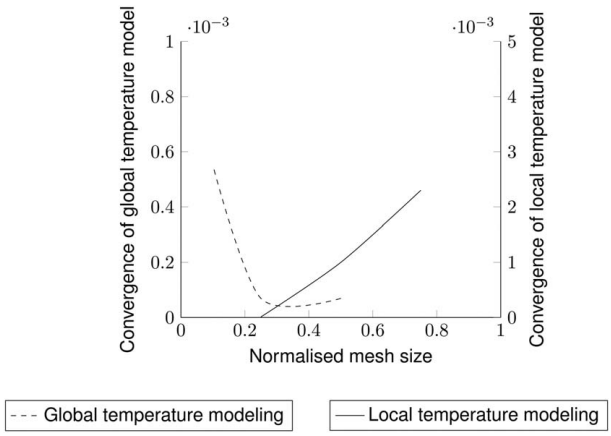

Fig. 7 Temperature convergence for different mesh sizes

Table 3 Global temperature results

Quantity	Surface loading model (°C)	Volumetric loading model (°C)	Analytical model (°C)
T_{surf}	1489	1374	1645
T_{TZM}	1197	1110	1226

and T_{TZM} from simulations are smaller than the values in analytical models by around 10%. Two reasons could explain this. First, the analytical model does not consider radiation boundary conditions. The second reason is the added heat transfer capacity from the extra thickness present in the actual design, as shown in Fig. 3, compared to the uniform cylinder used in the analytical model. There are additional differences in the numerical model from the temperature-dependent material properties used. The numerical model results without radiation were only 1% different from the ones with radiation. The spatial and temporal discretization errors were of the order of 0.1%. Hence, the discrepancy is predominantly due to geometrical details near the focal track and the temperature-dependent material properties that the analytical model could not capture. The values of T_{surf} and T_{TZM} from the volumetric heat loading model are lower by around 7–8% than the values of the surface heat loading modeling. This lower value in the volumetric heat loading model could be explained by the fact that the full power is not concentrated on the surface, like in the analytical and surface heat loading models. Thus, the volumetric heat loading analysis reduces the overestimating of peak surface temperatures for high-penetration-depth electron beam loading. The resulting global temperature distribution in the volumetric heat input model is shown in Fig. 8. As seen in the figure, the influence of the heat loading is only seen close to the outer radius of the target, near the focal track, due to the large radius and small electron beam loading time. The maximum temperature of TZM and tungsten occur almost at the same time, at the end of 1 s of electron beam radiation. While TZM has temperatures as high as 800 °C at a spot 4 mm away from the focal track, the temperature never exceeds ambient temperature from around 40 mm from the focal track in TZM, indicating that the thermal penetration in TZM is only limited to the outer edge near the focal track. The same simulations were repeated with the contact thermal resistance between the focal track and target body being made ten times higher. Since the resulting global temperatures were found to be higher by a maximum of only around 6%, the assumption of zero thermal resistance has been carried forward in this work.

6.4.3 Local Temperature Modeling. The results from the simulations for local temperature modeling with moving volumetric heat loading, explained in Sec. 6.3, are summarized in Table 4. The peak temperatures of tungsten, T_{peak}, from simulation and analytical model are compared. The values are lower in the simulation results than in the analytical model by around 7%. This could be explained by the same reasons as in the analysis of the global temperature modeling for T_{surf} because the analytical value of T_{peak} is the sum of T_{surf} and ΔT. The resulting temperature distribution after a time of 1 s in the local temperature modeling simulation is shown in Fig. 9. The top 100 μm layer of tungsten is the hottest as the electrons penetrate only this far. The influence of the heat from 200 μm below the top surface is minimal. The evolution of the temperature of the focal spot as the target rotates at a frequency of 175 Hz is shown in Fig. 10. Each temperature peak in Fig. 10 corresponds to the one rotation of the focal spot, and the final temperature reached at the end of 1 s corresponds to the maximum temperature of the focal spot T_{peak}. The value of T_{peak}, at 2108 °C, is much smaller than the melting point of tungsten, which is over 3400 °C, thus satisfying the requirement in Eq. (1). Additionally, Table 4 compares the local temperature rise ΔT from the analytical model with the temperature rise at the end of

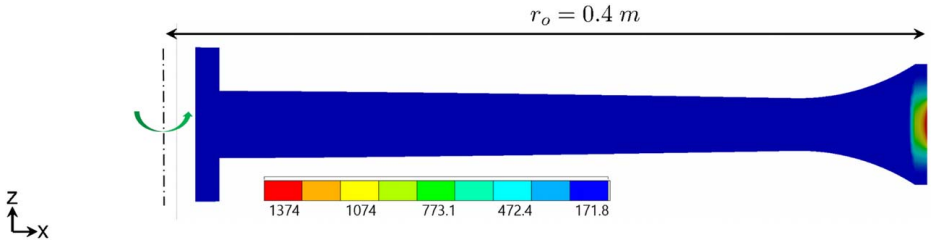

Fig. 8 Global temperature field in the radial half cross section of the target from the volumetric heat input model at time $t = 1$ s (°C)

Table 4 Results of the local temperature modeling

Quantity	Numerical model (°C)	Analytical model (°C)
ΔT	848	1036
T_{peak}	2107	2262

a time duration equal to the time taken for one focal spot width of 50 μm to be hit by electron beams as the target rotates, i.e., 4.4 μs. The temperature is also less than that of the analytical model because the simulation model considers radiation and heat transfer to the surrounding material. The local temperature increase computed by Eq. (10) is adiabatic at the instant of evaluation around the moving focal spot. Thus, no heat diffusion into the surrounding material is accounted for, which explains the higher temperature in the analytical model. Such a simulation, which can compute the temperature field around the focal spot in every rotation, will be used to compute the thermal stresses in the later sections.

7 Validation Method

7.1 Validation Strategy. A new validation strategy is being proposed to avoid the problem of lack of suitable test facilities discussed in Sec. 3.2. Even though the load case is created by an electron beam of a power of 1 MW with a flux of 1 TW m^{-2}, the state of the material created with this load case does not necessarily need such a powerful and concentrated electron beam. Typical high-heat-flux application validations apply electron beams on materials and compare parameters like stress, strain, and temperature to validate the capacity of the material to withstand the load case. The measurable quantities corresponding to these parameters include displacement, roughness, and surface temperatures [12]. While these are relevant quantities for this load case too, there could be an added

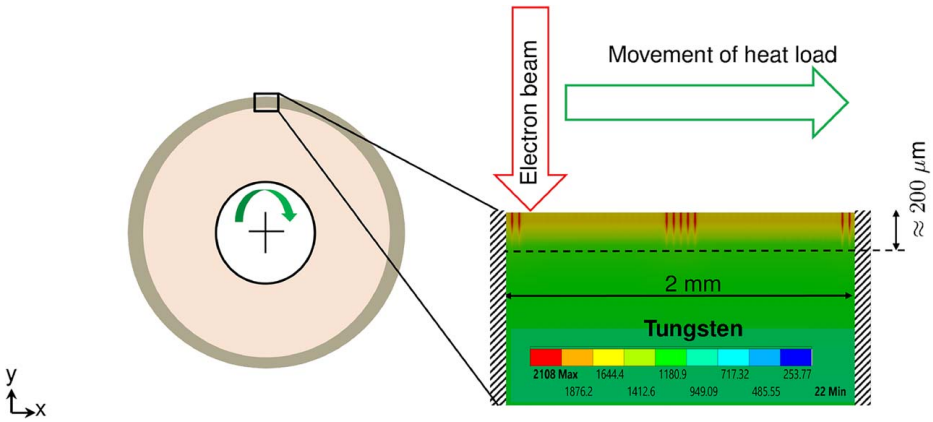

Fig. 9 Local temperature field at time $t = 1$ s (°C)

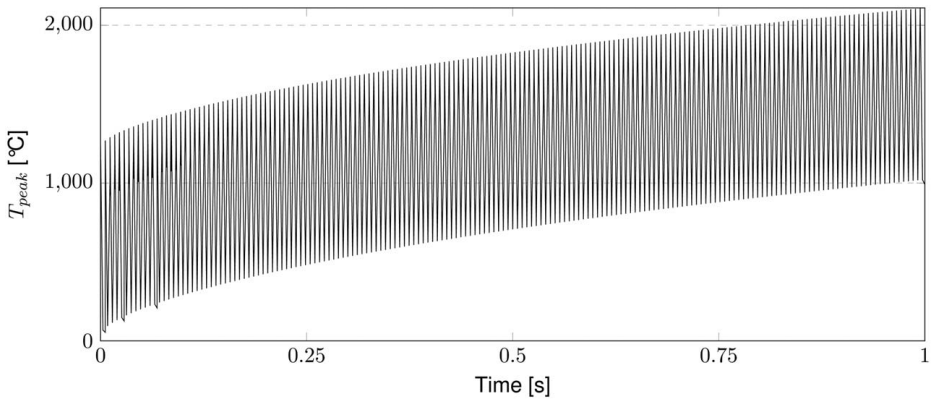

Fig. 10 Local temperature evolution with time

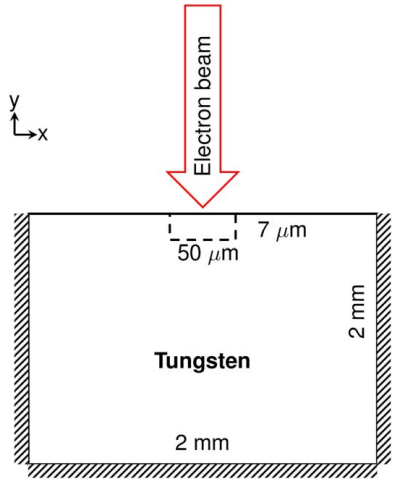

Fig. 11 Test setup in simulation with an electron beam penetration depth $d \approx 7\ \mu m$

quantity of interest, like strain rate. This is evident from Fig. 10 where the temperature rises from ambient temperature to above 1000 °C in around 0.1 μs. Such rapid temperature rise will be accompanied by a rapid thermal expansion and stress increase, and such a rapid structural expansion affects the material's performance since rapid expansion will affect the material's failure strength. In particular, tungsten and its alloys have been found to fail at much higher stress when loaded at high strain rates [27,28]. Hence, the critical quantities of interest that will be used to find a test method are identified to be von Mises stress σ, von Mises strain ε, temperature T, and strain rate $\dot{\varepsilon}$. Their requirements are laid out in Eqs. (11)–(14). The requirements for strain and strain rate are not an inequality constraint because higher strain and strain rate do not necessarily mean that the material is closer to failure. The upcoming section will elucidate the details of how a lower power test facility, already existing, could be used to match these requirements on the respective quantities of interest.

$$\text{Maximum } \sigma(x, t)_{lfxt} \leq \text{Maximum } \sigma(x, t)_{\text{test}} \tag{11}$$

$$\text{Maximum } T(x_{\sigma\max}, t)_{lfxt} \leq \text{Maximum } T(x_{\sigma\max}, t)_{\text{test}} \tag{12}$$

$$\text{Maximum } \varepsilon(x_{\sigma\max}, t)_{lfxt} \approx \text{Maximum } \varepsilon(x_{\sigma\max}, t)_{\text{test}} \tag{13}$$

$$\text{Maximum } \dot{\varepsilon}(x_{\sigma\max}, t)_{lfxt} \approx \text{Maximum } \dot{\varepsilon}(x_{\sigma\max}, t)_{\text{test}} \tag{14}$$

7.2 Numerical Model of the Proposed Validation Test. The numerical model of the moving volumetric heat input from Sec. 6.3 is used here to simulate a low-power electron beam validation test setup. The test specimen used is a small piece of tungsten in a setup as shown in Fig. 11. The mechanical boundary conditions are as shown as well, simulating the test equipment where the sample is clamped on all sides except the loaded top surface. A temperature-dependent, multi-linear plasticity model for tungsten alloy has been used in the simulation with temperature-dependent properties as listed in Tables 1 and 2 [25]. The FEM problem is solved as a coupled thermo-mechanical transient problem. The simulation is done for a particular time duration, sufficiently long to meet the requirements in Eqs. (11)–(14). The critical parameters like time, power, flux, and penetration depth are specified for both the lower power test and the original simulation in Table 5. The electron beam power is applied over the penetration depth homogeneously for the low-power test since the penetration depth is less than one-tenth of the original simulation. The power of the electron beam is comparable to an existing electron beam facility like JUDITH [15]. The power is also assumed to be applied over the same area of 0.05 mm × 20 mm for both models. The quantities of interest in both models will be compared in the simulation time mentioned in Table 5. Since the developed FEM model is not involving low-cycle fatigue material models and is yet to be validated using experimental results in the domain of operation, the scope of the work is to only establish an equivalence in the parameters between the test and real scenario over the simulation time as shown in Table 5. The aim of the designed experiment will be to repeat the pulse time in Table 5 over required number of cycles, matching the real scenario, thus inferring the low-cycle fatigue performance of the focal track and the ability to satisfy requirement given by Eq. (3). The simulation time for the original line-focus X-ray tube target for comparison has been chosen as the time taken for the width of the domain, 2 mm, to cross the electron beam impinging spot as it rotates.

Table 5 Simulation parameters for test and original requirement

Parameter	Test	LFXT
Time (s)	4.9×10^{-6}	4.4×10^{-6}
Power (MW)	0.08	1
Flux (TW m^{-2})	0.08	1
Penetration depth (μm)	7	100

7.3 Results and Inferences. The results of the simulation of the low-power electron beam test setup are compared with the results of the original line-focus X-ray tube target simulation from Sec. 6.4 in Table 6. The results are found to be comparable to or higher than the original requirement in the test setup simulation, satisfying Eqs. (11)–(14). Thus, a test facility with over ten times less power and flux can be used to create a material state as severe as the original scenario of a line-focus X-ray tube target when considering the key quantities of interest.

8 Summary and Outlook

In this work, the engineering requirements for an X-ray target to be used in MRT have been laid out. The critical differences in modeling and validation between state-of-the-art high-heat-flux-loaded components and the LFXT target for MRT were elucidated. Three different modeling strategies were proposed for the numerical modeling of the target. A validation strategy has been proposed to address the lack of existing test facilities to validate the material's ability to withstand thermal stresses. The key outcomes of the work are as follows:

(1) Tungsten focal track and target body material TZM can satisfy the thermal requirement by being sufficiently lower than their melting points.
(2) The volumetric heat source modeling results significantly differ from the surface heat source modeling results for such high-penetration electron beam loading applications.
(3) The feasibility of using an existing lower power test facility to validate the target for microbeam radiation therapy, without needing an electron beam facility of 1 MW power, has been established.

Furthermore, the results from the developed numerical model could be used for comparison with measurable quantities of interest like surface displacement and temperature, measured from the

Table 6 Simulation results for test setup and the LFXT

Parameter	Test	LFXT
Maximum T (°C)	2242	2107
Maximum σ (MPa)	487	440
Maximum ε	9×10^{-3}	4.8×10^{-3}
Maximum $\dot{\varepsilon}$ (s^{-1})	1.3×10^{3}	4.6×10^{3}

validation test. Such comparison will help improve the numerical model to match the test results more accurately. Thus, the numerical model can validate the target by simulating the original requirement of 1 MW more reliably. The modeling and validation method presented collectively establishes a strategy to design and validate an X-ray target for a novel high-power X-ray tube with ultra-high thermal loading requirements. The results presented in this work have identified a validation strategy based on a few key quantities of interest. In future research, the numerical model can be improved further to model a particular test facility, helping to identify the measurable quantities of interest along with their corresponding fields of measurement.

Acknowledgment

Albrecht Struppler Fellowship funded by the Federal Ministry of Education and Research (BMBF) and the Free State of Bavaria under the Excellence Strategy of the Federal Government and the Lä nder, as well as by the Technical University of Munich—Institute for Advanced Study, awarded to Dr. Kim Melanie Kraus, has funded parts of this research work.

Conflict of Interest

There are no conflicts of interest.

Data Availability Statement

The datasets generated and supporting the findings of this article are obtainable from the corresponding author upon reasonable request.

Nomenclature

b = focal track width (mm)
d = electron penetration depth (μm)
v = tangential velocity (m s^{-1})
E = Young's modulus (GPa)
P = electron beam power (W)
Q = heat flux (W m^{-2})
T = temperature (°C)
c_{Pw} = specific heat capacity of tungsten (J kg^{-1} K^{-1})
k_{TZM} = thermal conductivity of TZM (W m^{-1} K^{-1})
k_w = thermal conductivity of tungsten (W m^{-1} K^{-1})
r_o = target outer radius (m)
t_{op} = operation time (s)
t_w = focal track thickness (mm)
T_o = initial temperature (°C)
q' = dimensionless heat flux
Fo = Fourier number
FEM = finite element method
LFXT = line-focus X-ray tube
MRT = microbeam radiation therapy
PFC = plasma-facing component
TZM = titanium–zirconium–molybdenum alloy
α = thermal diffusivity (m^2 s^{-1})
ϵ = focal spot width (μm)
ε = von Mises strain
ρ = mass density (kg m^{-3})
σ = von Mises stress (MPa)

References

[1] Ravichandran, M., Winter, J., Dimroth, A., Bartzsch, S., Kraus, K. M., and Zimmermann, M., 2024, "Design and Validation Strategy for an X-Ray Target Subject to Ultra-High Heat Flux Loading," Heat Transfer Summer Conference, Anaheim, CA, July 15–17.
[2] Bouchet, A., Bräuer-Krisch, E., Prezado, Y., El Atifi, M., Rogalev, L., Le Clec'h, C., Laissue, J. A., Pelletier, L., and Le Duc, G., 2016, "Better Efficacy of Synchrotron Spatially Microfractionated Radiation Therapy Than Uniform Radiation Therapy on Glioma," Int. J. Radiat. Oncol. Biol. Phys., **95**(5), pp. 1485–1494.
[3] SIEMENS, 2012, "SIEMENS CT Scanner Specifications," https://s3.amazonaws.com/sgcimages/36_37_40_41_ITN1115_Siemens.pdf
[4] Bartzsch, S., and Oelfke, U., 2017, "Line Focus X-Ray Tubes: A New Concept to Produce High Brilliance X-Rays," Phys. Med. Biol., **62**(22), pp. 8600–8615.
[5] Winter, J., Galek, M., Matejcek, C., Wilkens, J. J., Aulenbacher, K., Combs, S. E., and Bartzsch, S., 2020, "Clinical Microbeam Radiation Therapy With a Compact Source: Specifications of the Line-Focus X-Ray Tube," Phys. Imaging Radiat. Oncol., **14**, pp. 74–81.
[6] Winter, J., Dimroth, A., Roetzer, S., Zhang, Y., Krämer, K.-L., Petrich, C., Matejcek, C., et al., 2022, "Heat Management of a Compact X-Ray Source for Microbeam Radiotherapy and Flash Treatments," Med. Phys., **49**(5), pp. 3375–3388.
[7] Wong, C., Woo, H., and Yap, S., 2007, "A Low Energy Tunable Pulsed X-Ray Source Based on the Pseudospark Electron Beam," Laser Part. Beams, **25**(3), pp. 497–502.
[8] Ravichandran, M., Winter, J., Bartzsch, S., and Zimmermann, M., 2022, "Material Selection for Extreme Thermo-mechanical Loads Using Design Space Projection: A Concept Study for an Ultra-High Power X-Ray Source," Proceedings of NordDesign 2022, Copenhagen, Denmark, Aug. 16–18.
[9] Li, M., Werner, E., and You, J.-H., 2015, "Influence of Heat Flux Loading Patterns on the Surface Cracking Features of Tungsten Armor Under Elmlike Thermal Shocks," J. Nucl. Mater., **457**, pp. 256–265.
[10] Zhukov, V. P., and Suslov, D. I., 2016, "Measurements and Modelling of Wall Heat Fluxes in Rocket Combustion Chamber With Porous Injector Head," Aerosp. Sci. Technol., **48**, pp. 67–74.
[11] Ahamed, S., and Kong, S.-C., 2024, "Analysis of Thermomechanical Stress of High-Temperature Ignition Surface Caused by Drop–Wall Interaction at Engine Conditions," ASME J. Therm. Sci. Eng. Appl., **16**(5), p. 051006.
[12] Li, M., 2015, "A Fracture Mechanics Study of Tungsten Failure Under High Heat Flux Loads," PhD thesis, Technische University Muenchen, Germany.
[13] Stupple, D. J., Kemp, V., Oldfield, M. J., Watts, J. F., and Baker, M. A., 2018, "Modeling of Heat Transfer in an Aluminum X-Ray Anode Employing a Chemical Vapor Deposited Diamond Heat Spreader," ASME J. Heat Transfer, **140**(12), p. 124501.
[14] Plankensteiner, A., and Roedhammer, P., 2001, "Finite Element Analysis of X-Ray Targets," Proceedings of the 15th International Plansee Seminar, Reutte, Austria, May 27–31, pp. 9–22.
[15] Wirtz, M., Linke, J., Pintsuk, G., Rapp, J., and Wright, G., 2012, "Influence of High Flux Hydrogen-Plasma Exposure on the Thermal Shock Induced Crack Formation in Tungsten," J. Nucl. Mater., **420**(1–3), pp. 218–221.
[16] Vasilij, G., Oleg, F., and Kolbasov, B., 2018, "Structural and Functional Materials: Selection Criteria and Radiation Characteristics," *Fundamentals of Magnetic Thermonuclear Reactor Design*, Elsevier, Sawston, UK, pp. 387–400.
[17] Sumi, N., Hetnarski, R. B., and Noda, N., 1987, "Transient Thermal Stresses Due to a Local Source of Heat Moving Over the Surface of an Infinite Elastic Slab," J. Therm. Stresses, **10**(1), pp. 83–96.
[18] Hetnarski, R. B., 2014, "Moving Heat Sources," *Encyclopedia of Thermal Stresses*, Springer Dordrecht, Dordrecht, Netherlands, pp. 3215–3227.
[19] Fox, N., 1965, "Thermal Stresses Due to a Moving Line Source on a Plane Boundary," Q. J. Mech. Appl. Math., **18**(1), pp. 25–30.
[20] Ayyadevara, N. T., Subramanian, B., and Meda, N. S., 2022, "Experimental and Computational Investigation for Accelerated Testing and Characterization of Next-Generation Steam Turbine Rotors," ASME J. Therm. Sci. Eng. Appl., **14**(12), p. 121011.
[21] Linsmeier, C., Unterberg, B., Coenen, J., Doerner, R., Greuner, H., Kreter, A., Linke, J., and Maier, H., 2017, "Material Testing Facilities and Programs for Plasma-Facing Component Testing," Nucl. Fusion, **57**(9), p. 092012.
[22] Wirtz, O. M., and Singheiser, L., 2012, "Thermal Shock Behaviour of Different Tungsten Grades Under Varying Conditions," PhD thesis, Forschungszentrum, Zentralbibliothek.
[23] Plansee, 2023, "Refractory Metals," https://www.plansee.com/en/materials.html
[24] Klopp, W. D., Witzke, W. R., and Raffo, P. L., 1966, *Mechanical Properties of Dilute Tungsten-Rhenium Alloys*, National Aeronautics and Space Administration, Cleveland, OH.
[25] Ryan, K. F., and Dowding, R. J., 1993, "Yield Properties of Tungsten and Tungsten Heavy Alloys," Army Research Laboratory, ARL-TR-143.
[26] Incropera, F. P., DeWitt, D. P., Bergman, T. L., and Lavine, A. S., 1996, *Fundamentals of Heat and Mass Transfer*, Vol. 6, Wiley, New York.
[27] Škoro, G., Bennett, J., Edgecock, T., and Booth, C., 2012, "Yield Strength of Molybdenum, Tantalum and Tungsten at High Strain Rates and Very High Temperatures," J. Nucl. Mater., **426**(1–3), pp. 45–51.
[28] Cadoni, E., Dotta, M., and Forni, D., 2020, "High Strain-Rate Behaviour of a Tungsten Alloy," Procedia Struct. Integrity, **28**, pp. 964–970.